

Systematic studies of pulse propagation in ducted oceanic waveguides in normal mode representation

N.A. Sidorovskaia^a

Physics Department, University of Louisiana at Lafayette, USA

Received: 24 February 2003 / Received in final form: 5 September 2003 / Accepted: 20 October 2003
Published online (Inserted Later) – © EDP Sciences

Abstract. Acoustic pulse propagations in typical environments of the Gulf of Mexico and Yellow Sea are modeled by a new normal mode code, SWAMP, and compared to the experimental data. The presence of the seasonal surface duct in the ocean is confirmed to be responsible for the generation of a unique set of modes forming the so-called “Precursor Phenomenon” first discovered by DeFerrari and Monjo. It is shown that the conventional theory of group velocity fails to predict precursor’s arrival time. Two different approaches, the mean rate of energy transport and Airy-wave analysis, are proposed for the description of the actual physical process of energy transport by precursors. The influence of the range-dependent bathymetry on a precursor structure is addressed. The presence of precursors appears to be sensitive to range dependence and may be diminished due to rapidly changing bathymetry. Based on numerical results, inversion procedures of extracting different environmental and source parameters from a received pulse structure are discussed.

PACS. 43.30.Bp Normal mode propagation of sound in water – 43.30.Pc Ocean parameter estimation by acoustical methods; remote sensing; imaging, inversion, acoustic tomography

1 Introduction

The propagation of acoustic signals of limited duration – *pulses* – in an ocean waveguide has more complicated and more informative features in comparison with the propagation of monochromatic waves. The analysis of the time-domain pulse structure at some distance from a source can give a variety of information (obtained remotely) about a radiating source and environment, such as source location, vertical sound speed profile in a water column, the presence of range-dependence along a propagation path, bottom properties, etc. [1–5]. The solution of an *inverse* problem for the determination of ocean and bottom properties given the properties of the transmitted and received signals is of considerable interest in physical oceanography, ocean acoustic tomography and seismology [5–8]. The application of any sophisticated inverse method requires a reasonable understanding of the physics of the forward problem.

The impetus of writing this paper was a new phenomenon observed in the acoustic experiments in the Straits of Florida. It was found in an experimental acoustic data set, collected as a part of the Subtropical Atlantic Climate Studies (STACS) in the Florida Straits in 1983, that slight seasonal variations of the temperature near the ocean surface, forming an additional weak surface duct, can generate unique features in the arrived pulse

structure [9,10]. (Term “surface duct” is associated with the presence of the local minimum in the sound speed profile near ocean surface.) This acoustic data set represents a great opportunity to understand the physics of the shallow water surface duct propagation, which has been paid far less attention than it deserves. The first range-independent modeling for this effect was conducted by Monjo using ray and full-wave computer models. He, together with DeFerrari, has proposed an empirical model describing the mechanism of energy trapping in the surface duct, when the source and receiver were far below the duct [9,10]. The present study, based on general pulse propagation theory in terms of the normal mode representation, offers a systematic computer simulation of the experimentally observed effect for various typical ocean environments. The importance of the development of a new mathematical model for the prediction of energy arrival times due to duct is also addressed. The pulse arrival parameters predicted by the model are in a good agreement with the experimental ones. The new normal mode algorithm, implemented in the recently developed modal program SWAMP (Shallow Water Acoustic Modal Propagation) [11,12], has shown to be very effective in inferring the physics responsible for forming the particular pulse structure. Systematic modeling and comparison of the bottom (single) and surface-bottom (double) duct environments with possible range-dependent propagation paths have allowed to conclude that the effect of the

^a e-mail: nsidorovskaia@louisiana.edu

seasonally-formed double-duct environment can be used for gaining more information about source location and environmental changes along a propagation path.

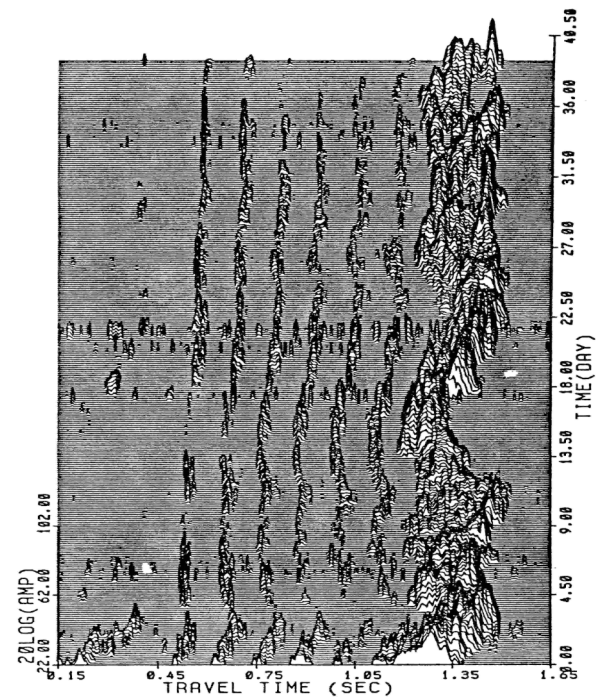
2 Acoustic experiment and environmental model

First, the effect that initiated this study during author's visit at the Rosenstiel School of Marine and Atmospheric Sciences of the University of Miami will be described. The experiment description closely follows Monjo and reproduces some experimental records from his dissertation [10]. The phenomenon was first observed and well documented in the October 1983 Florida Straits experiment. For the experiment three transceivers (1, 2, 3) were deployed 38 m above the bottom in about 550 meter deep water. The moorings were approximately 42 km apart. Path 1–2 was nearly flat (range-independent) with the average depth of 550 m. The other two paths (2–3 and 1–3) traversed range-dependent bathymetry. The sound speed profile was measured to be relatively range-independent. The weak surface duct appeared in October experiment. Data sets consist of six sets of channel responses, sampled every hour for a 40-day period. One mooring would transmit a 4-cycle sinusoidal pulse at a carrier frequency of 459.558 Hz while the other two moorings recorded the incoming pulse. Then after 5 minutes, a second mooring transmitted while the other two recorded. Finally, the third would transmit, ending one complete cycle. The cycle was repeated every hour. The received data on every mooring were bandpassed, amplified, complex demodulated, and finally coherently averaged over every 135 complex demodulated sequences. This processing removed the carrier frequency and averaged out the incoherent part of the signal. The Doppler shifted surface scattered energy is not present in the final records and cannot contribute to the observed effects.

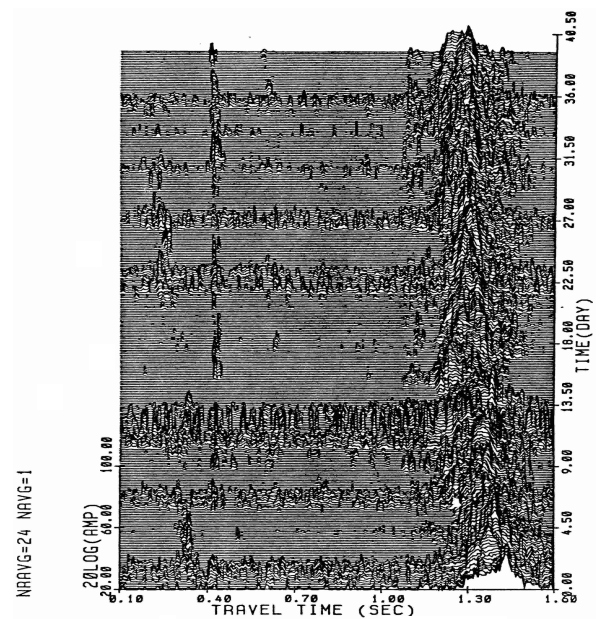
Two typical October data sets for range-independent and range-dependent bathymetries are presented in Figures 1a and b, respectively.

Each data set shows a late main peak of high intensity with several earlier discrete arrivals, which were referred to as precursors by DeFerrari and Monjo [9]. The precursors were unexpected and had not been observed during the August experiment when the surface duct had been absent. Six precursors are evident for the range-independent path, but only the first fastest one can be readily observed for the range-dependent case. The time lag between any two adjacent precursors was the same and did not vary during 40 day period. It shows the presence of a very typical deterministic effect of the ocean channel, which needs to be understood.

An understanding of the physics of these six precursors requires one to choose the simplest numerical model, which describes the essential features of this propagation channel, responsible for the precursor formation. Using the direct sound speed measurements obtained during the experiment, the complete *basic* model used as an input



(a)



(b)

Fig. 1. Experimental data for: (a) range-independent path, (b) range-dependent path. (Reproduced from [9,10].)

for modeling by a new normal mode code, SWAMP, is shown in Figure 2. These input parameters represent a simplified way of estimating the average conditions in the experiment.

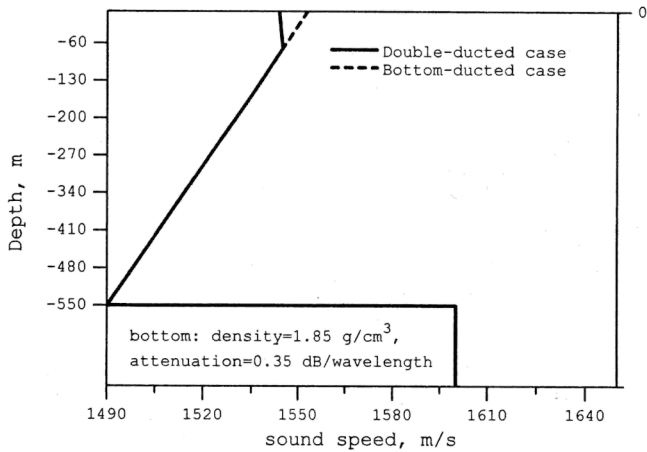


Fig. 2. Environmental model for SWAMP.

3 Pulse propagation modeling in SWAMP

Within the framework of linear acoustics there are two fundamental approaches to modeling pulse propagation in an ocean waveguide. One solves the problem directly in the time-domain, which, however, requires the development of an entirely new set of propagation codes [13–15]. The second approach widely used in underwater acoustics is to solve the pulse propagation problem via the frequency domain by Fourier synthesis of CW (Continuous Wave) results [11, 16]. The second approach allows linking any of the time-harmonic acoustic models with the algorithm of the Fourier synthesis, giving the pulse response. This method is implemented in the extended version of SWAMP, which includes both CW and the Fourier synthesis blocks. In this section a brief overview of a new normal mode approach used in SWAMP and the theory of pulse propagation will be detailed for a use in the analysis of the effect observed in the Florida Straits experiment.

3.1 SWAMP overview

To describe the propagation of CW signal through arbitrary oceanic waveguide, one is facing a problem of the solution of the Helmholtz equation with complicated boundary conditions and variable sound speed profiles. There are only a few relatively simple waveguides, which allow one to obtain a closed analytical form of the solution describing sound propagation in them. All other environments require a use of numerical acoustic models based on mathematical approximations. Among various numerical solution strategies, implemented in different numerical models, the normal mode (NM) approach is the fastest and most effective one for range-independent waveguides (sound speed profile depends only on a depth coordinate and bathymetry is flat). The important advantage of using NM-algorithm is the possibility of easy physical interpretation of the results and development of inversion procedure to infer the information about a source and a waveguide from the array detected signals. There are now

several one-way and two-way coupled modal schemes implemented in computer codes for range-dependent cases. Once the sound speed profile becomes nonlinear and range dependent, most existing NM codes employ the Finite-Difference Methods (FDM) to solve the depth-separated (modal) equation. This procedure could be very computationally intensive. This puts existing NM acoustic models far behind Parabolic Equation (PE) algorithms in the computational time competition. The challenge behind a design of a new normal mode algorithm was to increase the analytical component in the solution of modal equation for an arbitrary sound speed profile that would also allow the coupling procedure to become more computationally effective.

The approach in SWAMP algorithm is a new one, based on representing the solution of modal equation in terms of spanning functions from the solution for an iso-velocity waveguide that is in some average sense close to the variable profile and using elements of the Sturm-Liouville theory. In the following discussion the only analytical part of SWAMP model is presented, the details of effective computational implementation could be found are in [11]. At this point two ocean models with the same bottom properties will be examined. One model has an iso-velocity water column while the other has a variable velocity profile. The bottom properties are the same approximated by multi-layered fluid medium. The set of water column propagating modes for the depth-separated wave equation for the iso-velocity water column subject to the certain boundary conditions is obtained first. It is expressed as a solution of Helmholtz's equation:

$$\frac{\varphi_{0m}}{dz^2} + \{k_0^2 - \lambda_m^0\} \varphi_{0m} = \frac{\varphi_{0m}}{dz^2} + \alpha_m^2 \varphi_{0m} = 0, \quad m = 1 \div M_0. \quad (1)$$

The equation that governs the solution for mode U_m in the water column for an arbitrary sound speed profile is:

$$\frac{U_m}{dz^2} + \{k^2(z) - \lambda_m\} U_m = 0. \quad (2)$$

The terms in equation (2) can be rearranged in such a way that the left-hand side of the equation contains the operator for the iso-velocity case:

$$\frac{U_m}{dz^2} + \{k_0^2 - \lambda_m^0\} U_m = QU_m, \quad (3)$$

where $Q = k_0^2 - k^2(z) - \lambda_m^0 + \lambda_m = q(z) + \Delta\lambda$. Recall that for the Sturm-Liouville problems we have the orthogonality condition:

$$(\varphi_i, \eta\varphi_j) = \int_0^{h_0} \eta_0 \varphi_{oi}(z) \varphi_{oj}(z) dz + \sum_{l=1}^{L-1} \int_{h_l}^{h_{l+1}} \eta_l \varphi_{li}(z) \varphi_{lj}(z) dz = \delta_{ij} n_i^2 \quad (4)$$

for any two functions φ_i and φ_j , which represent the solution spanning the whole multi-layered medium with a

constant sound speed within a particular bottom layer, l . $\eta_l = 1/\rho_l$, if Helmholtz's equation is written for pressure, or $\eta_l = \rho_l$, if it is for the displacement potential (ρ_l is a fluid density in a layer, l). Let us assume completeness of the space, namely, that the eigenfunctions of the iso-velocity space represent the complete set of basis function for the variable velocity space. Then, in particular, within the water column we can decompose the solution for the variable velocity space as:

$$U_m = \sum_{j=1}^{M_0} a_{mj} \varphi_{0j}. \quad (5)$$

Substituting series (5) in equation (3) and using equation (1), one obtains:

$$\sum_{j=1}^{M_0} a_{mj} (\alpha_m^2 - \alpha_j^2) \varphi_{0j} = \sum_{j=1}^{M_0} a_{mj} (q(z) + \Delta \lambda_m) \varphi_{0j}, \quad m = 1 \div M. \quad (6)$$

The number of modes M for the variable velocity profile problem has to be determined by requiring that a mode has to be perfectly trapped in the water column. Multiplying both sides of equation (6) by $\eta_0 \varphi_{0k}$ and integrating over only the water column, one arrives at:

$$\lambda_m \sum_{j=1}^{M_0} a_{mj} b_{jk} = \lambda_m^0 \sum_{j=1}^{M_0} a_{mj} b_{jk} - \sum_{j=1}^{M_0} a_{mj} q_{jk} + \alpha_m^2 \sum_{j=1}^{M_0} a_{mj} b_{jk} - \sum_{j=1}^{M_0} a_{mj} \alpha_j^2 b_{jk}, \quad (7)$$

where

$$q_{jk} = \int_0^{h_0} \eta_0 q(z) \varphi_{0j}(z) \varphi_{0k}(z) dz$$

and

$$b_{jk} = \int_0^{h_0} \eta_0 \varphi_{0i}(z) \varphi_{0j}(z) dz,$$

which can be calculated as soon as one has solved the iso-velocity problem, so at this stage they are known. Set of equation (7) can be written in a matrix form as follows:

$$\mathbf{\Lambda} \mathbf{A} \mathbf{B} = \mathbf{\Lambda}^0 \mathbf{A} \mathbf{B} - \mathbf{A} \mathbf{Q} + \mathbf{K} \mathbf{A} \mathbf{B} - \mathbf{A} \mathbf{K} \mathbf{B}, \mathbf{K} = \alpha_m^2 \mathbf{I}, \quad (8)$$

where \mathbf{I} is the identity (unit) matrix. Matrices \mathbf{Q} and \mathbf{B} are both symmetric. Here $\mathbf{\Lambda}$, $\mathbf{\Lambda}^0$, and \mathbf{K} are diagonal matrices of the respective eigenvalues, where the diagonal term for row m is the eigenvalue λ_m , λ_m^0 , and α_m^2 , respectively.

Equation (8) is actually a generalized eigenvalue problem which may be reduced to the following form by using the fact that $\mathbf{\Lambda}^0 + \mathbf{K} = \mathbf{k}_0^2 \mathbf{I}$:

$$\mathbf{\Lambda} \mathbf{A} \mathbf{B} = \mathbf{k}_0^2 \mathbf{I} \mathbf{A} \mathbf{B} - \mathbf{A} \mathbf{K} \mathbf{B} - \mathbf{A} \mathbf{Q} = \mathbf{\Lambda} \mathbf{\Lambda}^0 \mathbf{B} - \mathbf{A} \mathbf{Q}. \quad (9)$$

Equation (9) can be solved by post multiplying both sides by the inverse of \mathbf{B} to arrive at a matrix, which

is not generally symmetric. One then may make a use of the QR-algorithm [17] for general non-symmetric or non-Hermitian matrices, which gives both the eigenvalues and the eigenfunctions at somewhat more computational cost than if one had a symmetric matrix. In the final SWAMP implementation the problem was transformed to one of symmetric form, which is computationally more effective and mathematically more aesthetic. (Refer to details in [11].) The coupling procedure for range dependent bathymetry currently employed is SWAMP is traditional one-way coupling neglecting the weak backscattering component [18]. The computational time for mode coupling has been greatly reduced due to the analytical form of solution (5), since the transfer matrices across vertical interfaces may be constructed analytically. This allows the code to be very competitive with the PE-models in computational speed for range-dependent environments. The range independent and range dependent versions of SWAMP were favorably benchmarked against NAVY standard propagation codes [2, 11]. The final significant remark about SWAMP is the fact that the waveguide solution implemented in code could be analytically transformed into a spherical representation. (Solution (5) contains only sinusoidal trigonometric functions.) This representation is essential if a target scattering effect needs to be incorporated into the model. The operator or matrix that transforms the incident field into the scattered field is referred to as a Transition matrix, or T-matrix [19]. The important point is that the T-matrix is a third rank tensor in the spherical representation, so any incident field must be expressed in the same representation in order to map it onto the scattered field. Hence, the target scattering can be incorporated into SWAMP making it a potentially unique tool for evaluating scattering and reverberation scenarios present in experimental data.

3.2 Pulse model for SWAMP

The extended version of SWAMP contains the Fourier synthesis block to simulate the pulse temporal response. Let the time dependence of the model source function be given by a real function $s(t)$. For the experiment of interest the function $s(t)$ is:

$$s(t) = \begin{cases} \cos(2\pi f_0 t), & 0 \leq t \leq t_s = \frac{N_T}{f_0} \\ 0, & t > t_s \end{cases}, \quad (10)$$

where f_0 is the carrier frequency, t_s is the temporal interval of the active radiating status of a transceiver defined by a parameter N_T , the number of periods of the cosine in the active signal. The simulated temporal pulse response at particular spatial point, (r, z) , in a waveguide can be obtained via the inverse Fourier transform of the frequency domain solution:

$$p(r, z, t) = \frac{1}{2\pi} \int_0^{w_{\max}} S(w) p(r, z, w) e^{-iwt} dw + c.c., \quad (11)$$

where $S(w)$ is the spectrum of $s(t)$, $p(r, z, w)$ is the spatial transfer function (Green's function), and the symbol *c.c.*

denotes the complex conjugate of the first term. $p(r, z, w)$ is generated by the CW block of SWAMP at a number of discrete frequencies within the frequency band of interest. When $s(t)$ is a real function, then

$$S(-w) = S^*(w), \quad (12)$$

where $S^*(w)$ is the complex conjugate of $S(w)$. It can be readily verified that the solution of the Helmholtz equation is conjugate symmetric. It is assumed in equation (11) that the source does not emit any significant energy above a certain frequency w_{\max} . This was true for the experiment because the radiated signal had a bandwidth of 115 Hz, which corresponds to the main spectral lobe of $S(w)$. In addition, at the receiver the signal was bandpass filtered using the same bandwidth. The spectrum of the function $s(t)$ is:

$$\begin{aligned} S(w) &= \int_{-\infty}^{\infty} s(t)e^{iwt} dt = \int_0^{t_s} \cos(w_0 t) e^{iwt} dt \\ &= e^{i(w_0+w)t_s/2} \frac{\sin(w+w_0)\frac{t_s}{2}}{w+w_0} \\ &\quad + e^{i(w-w_0)t_s/2} \frac{\sin(w-w_0)\frac{t_s}{2}}{w-w_0}. \end{aligned} \quad (13)$$

The shape of the radiated spectrum suggests that most of the energy lies within the main lobe of the function $\text{sinc}(x) = \sin(x)/x$, $x = (w-w_0)\frac{t_s}{2}$. The first nulls of this function give the main frequency band:

$$f_0 - \frac{1}{t_s} \leq f \leq f_0 + \frac{1}{t_s}, \quad t_s = \frac{N_T}{f_0}. \quad (14)$$

In this representation N_T can be manipulated to reproduce a bandwidth of the actual source.

The spatial transfer function at a particular frequency written in the form of a superposition of normal modes is [16]:

$$\begin{aligned} p(r, z, w) &= \sum_m \phi_m(w, r, z) \\ &= \sum_m \psi_m(z, z_s, w, \lambda_m) H_0^{(1)}(k_{rm} r), \end{aligned} \quad (15)$$

where $k_{rm} = \sqrt{\lambda_m}$, $\phi_m(w, r, z)$ can be viewed as the field of an individual normal mode, $\psi_m \propto U_m(z)U_m(z_s)$ is proportional to the product of vertical modal function and the excitation coefficient for mode m corresponding to the vertical wavenumber $\sqrt{k^2(z) - k_{rm}^2}$, and $H_0^{(1)}$ is the Hankel function of the first kind of order zero. Equation (15) corresponds to a range-independent environment. There is no reasonably simple analytic form for range-dependent media, so they must be investigated primarily by means of numerical simulations. Substituting equation (15) into equation (11) and changing the order of integration and summation, one obtains for arbitrary r, z , and t :

$$p(r, z, t) = \sum_m \Phi_m(r, z, t), \quad (16)$$

where $\Phi_m(r, z, t) = \frac{1}{2\pi} \int_0^{w_{\max}} S(w) \phi_m e^{-iwt} dw + c.c.$, which can be called the *pulse field of the individual normal mode*. Using the asymptotic representation for the Hankel functions at sufficiently large distances ($k_{rm} r \gg 1$), one can rewrite the pulse field of the individual mode in the far field as:

$$\Phi_m(r, z, t) = \frac{1}{2\pi\sqrt{r}} \int_0^{w_{\max}} S(w) \psi_m \frac{e^{i(k_{rm} r - wt)}}{\sqrt{k_{rm}}} dw + c.c. \quad (17)$$

The following analysis of the integral in (17) and common physical intuition tell that at any arbitrary receiver point the measured pulse response represents the result of the distortions of the original signal, equation (10), by the ocean medium. For a particular receiver location all the distortions can be represented by introducing the *amplitude* $a(t)$ and *phase modulation* $\theta(t)$ of the original signal with carrier frequency $w_0 = 2\pi f_0$ [5]:

$$p(t)|_{z,r} = a(t) \cos[w_0 t + \theta(t)]. \quad (18)$$

For signals with bandpass spectra, which is usually the case for experimental data, it is convenient to define the *complex envelope function* of the signal which contains the information about the waveguide parameters and will be analyzed in the following numerical studies. Expanding the cosine in equation (18), one arrives at:

$$\begin{aligned} p(t)|_{z,r} &= a(t) [\cos \theta(t) \cos w_0 t - \sin \theta(t) \sin w_0 t] \\ &= 2p_x(t) \cos w_0 t - 2p_y(t) \sin w_0 t, \end{aligned} \quad (19)$$

where p_x and p_y are the in-phase and quadrature components of the signal. Combining them into a single complex number gives the complex envelope, $p_c(t)$:

$$p_c(t)|_{z,r} = p_x(t) + ip_y(t) = \frac{1}{2} a(t) e^{i\theta(t)}. \quad (20)$$

The received (or modeled) signal can be written as:

$$p(t)|_{z,r} = p_c(t) e^{iw_0 t} + p_c^*(t) e^{-iw_0 t}. \quad (21)$$

The complex envelope can be obtained by multiplying the received signal by $e^{-iw_0 t}$:

$$p(t)|_{z,r} e^{-iw_0 t} = p_c(t) + p_c^*(t) e^{-i2w_0 t} \rightarrow p_c(t), \quad (22)$$

where the last arrow indicates that the signal has been low-pass-filtered to remove the double-frequency components. In the experiment, if one deals with an unknown signal, which implies some kind of passive analysis, one has some freedom in the choice of the demodulation frequency w_0 . If the nature of the radiated signal is known, the selection of the carrier frequency for carrier-borne signals as demodulation one simplifies the analysis. In the time-domain part, added to SWAMP for modeling pulse signal propagation via the Fourier synthesis, a computationally simple approach of choosing the input sample rate

Δt for the signal discretization in equation (10) to be four samples per carrier cycle is used:

$$s(t_j = j\Delta t) = \begin{cases} \cos(2\pi f_0 t_j), & \text{if } t_j \leq t_s = \frac{N_T}{f_0} \\ 0, & \text{if } t_s < t \leq T = \Delta t N_F \end{cases}, \quad (23)$$

where $\Delta t = \frac{1}{4f_0}$, and zero-filling is implied for the rest of the digitized signal to reach the desired resolution in the frequency domain. For the particular choice of Δt the multiplication by

$$e^{-iw_0 t_j} = e^{-i2\pi f_0 \frac{j}{4f_0}} = e^{-i\frac{\pi}{2}j} = (-i)^j \quad (24)$$

in equation (22) for the integer j can be reduced to multiplication by $\{1, -i, -1, i\}$. Low-pass filtering to remove the double frequency components is performed by a non overlapping block average over $N = 4$ values. It is important to mention that this filter has sidelobe effects, so sometimes it is preferable to use the Gaussian filter.

Once the original signal and the spatial transfer function are sampled, N_F can be chosen to be an integer power of 2, and then the so-called *Fast Fourier Transform* (FFT) can be implemented for evaluating the discrete analog of equations (11) or (17). In the numerical algorithm one should be careful about the choice of parameter N_F . This parameter gives the relation between sampling in the time and frequency domains from the discrete Fourier transform theory [17]:

$$\Delta t \Delta w = \frac{2\pi}{N_F}. \quad (25)$$

It is important to relate the frequency sampling to the maximum frequency content of the source signal:

$$\frac{1}{2} N_F \Delta w \geq w_{\max}. \quad (26)$$

Using (25), it is evident that this inequality is identical to the *Nyquist criterion* for the sampling frequency f_s :

$$f_s = \frac{1}{\Delta t} \geq 2f_{\max}. \quad (27)$$

By choosing the filter properties (14) and the sampling rate (23), condition (27) is satisfied in the model. However, this is only one aspect of the problem. In addition, the time window has to serve the observation goals, and it must be selected large enough that it contains the entire transient pulse response at each given receiver to eliminate the *wrap-around* effect. It turns out that all of the received pulse energy that lies outside the given temporal window is falsely translated into the observation window by the very act of discrete sampling, so one wants to be sure that most of the arrived energy fits into the given temporal interval [17,18]. The duration of the transient response is controlled by both the source parameters and dispersive nature of an ocean waveguide. The selection of the time window should be done in accordance with the waveguide parameters, which clearly makes it quite difficult for complicated environments. For long-range propagation one can estimate the minimum rate u_{\min} of energy

transport in the frequency interval of interest and select the time window $T = N_F \Delta t$ such that he could see the complete pulse response at the farthest receiver range, i.e.,

$$T = t_{\max} - t_{\min} \geq r_{\max} \left\{ \frac{1}{u_{\min}} - \frac{1}{c_{\max}} \right\}. \quad (28)$$

A conservative estimate of the fastest arrivals corresponding to t_{\min} is determined by the highest sound speed in the problem. Those arrivals are usually related to the sound speed in the bottom. It was found that for the model in Figure 2 a time window of about 2 seconds is adequate for propagation ranges up to 50 km. Hence, the length of the FFT is equal to 4096.

4 Numerical simulation results for range-independent Florida Straights environment

Several different environmental parameter sets were investigated not only to simulate the results observed in the experiment, but also to conduct systematic studies of the precursor phenomenon. The input model with surface and bottom ducts shown in Figure 2, describing the average experimental conditions, will be referred to as the basic model. Any variations from the basic model parameters will be pointed out in the following discussion.

Figures 3 and 4 show SWAMP-modeled pulse responses for the basic model throughout the water column over a 2.3 second time interval at two fixed ranges, 42 and 20 km.

Figure 5 shows the pulse response when the surface duct is absent, so there is a linear decrease of the sound speed throughout the water column from 1553 m/s at the surface to 1490 m/s at the bottom, i.e., only the bottom duct is present. The gradient used for the bottom duct is about -0.115 m/s/m and for the surface duct is about $+0.016$ m/s/m.

Comparison of the single and double duct cases shows a noticeable differences in temporal distribution of the arrived acoustic energy, despite the one seventh weaker gradient for the surface duct. The surface duct associated energy arrives 0.6 seconds before the energy trapped in the bottom duct. The SWAMP results predict all six discrete precursors at 42 km, and the temporal delay between precursors compares well with experimentally observed ones: the ducted arrivals are evenly spaced in time, about 0.09 seconds apart. (Refer to Figs. 1a and 3.) A simpler bottom model than Monjo's one [9,10] was used for modeling but the effect is still well-observed. It means that the bottom structure is not responsible for the phenomenon formation. However, as is evident from the simulation results presented below, the geoacoustic input model partially contributes to both the relative and absolute amplitudes of the precursors.

To interpret the broadband SWAMP results, let us compare vertical modal functions for the double-ducted and bottom-ducted waveguides. Lower modes 1 and 9

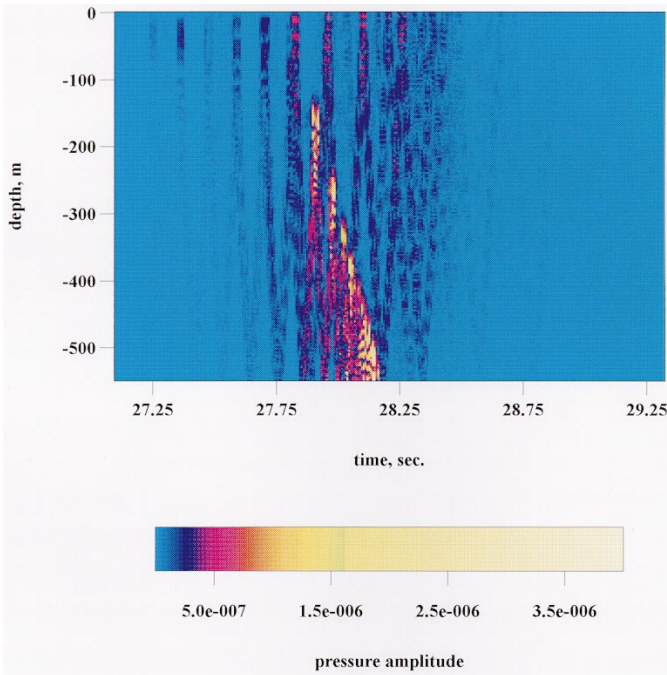


Fig. 3. Pulse response at the range of 42 km for double-duct environment.

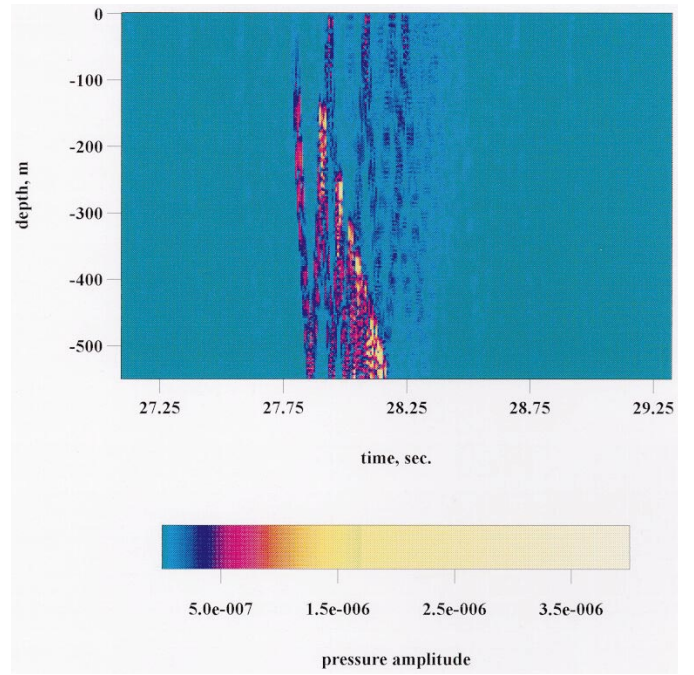


Fig. 5. Pulse response at the range of 42 km for single-duct environment.

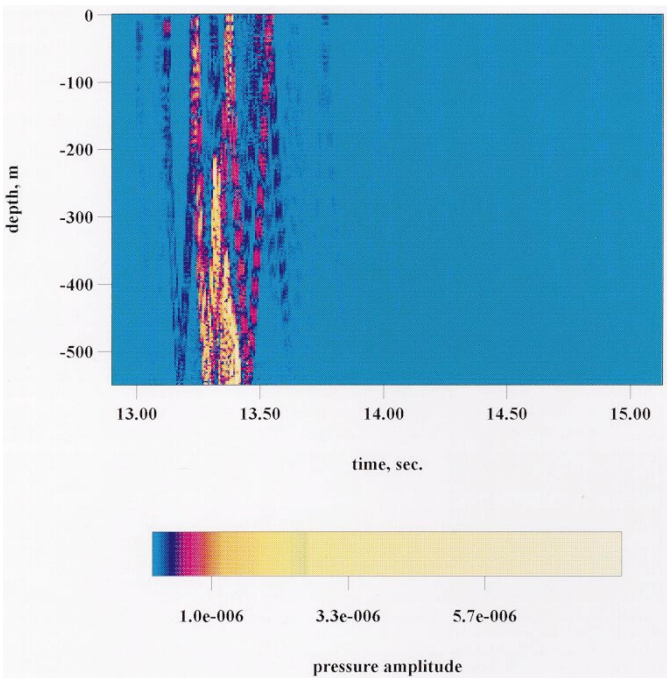


Fig. 4. Pulse response at the range of 20 km for double-duct environment.

for the double-ducted waveguide at 460 Hz are shown in Figures 6a and 6b. Their shapes are identical to the linear case. Thus, the lower-order modes are trapped in the bottom duct and form the most powerful arrival energy peak in Figures 3 and 4. A unique series of modes in the presence of the surface duct corresponds to mode numbers 50–60. Only mode 53 (Fig. 6c) is nearly perfectly

trapped in the surface duct, while other modes from this series (as in Fig. 6d) are partially trapped, leaking energy to the bottom. The mechanism of the energy leakage to the bottom provides an opportunity to observe the precursors even at receivers which are placed in the bottom duct as they were in the experiment. The high-order modes are uniformly distributed through the water column (see Fig. 6e) and intensively interact with the bottom. Thus, they are the most attenuated with the longest travel paths. They carry the pulse energy that arrives at the “tail” of the pulse, and is expected to contain information about bottom properties.

Figure 7 shows the vertical structure of mode 53 in the bottom-ducted waveguide. The comparison to Figure 6c shows that the presence of the surface duct crucially changes the shape of this mode. The number of the mode associated with the perfect trapping in the surface duct changes with increasing frequency. Figure 8 presents a perfectly trapped mode at 526 Hz. The mode number is 60.

One can clearly see that the “quality” of trapping improves as frequency increases. Color maps of transmission loss versus depth and range for 460 Hz and 526 Hz are presented in Figures 9a and 9b.

These plots demonstrate once again that the retention of energy in the surface duct improves with increasing frequency. As a conclusion, energy trapping in the surface duct is more pronounced at higher frequencies and absent at low frequencies. This fact also implies that the high frequency operations in shallow water with surface duct should be considerably influenced by this phenomenon. The numerical results, presented in Section 5, will confirm this statement.

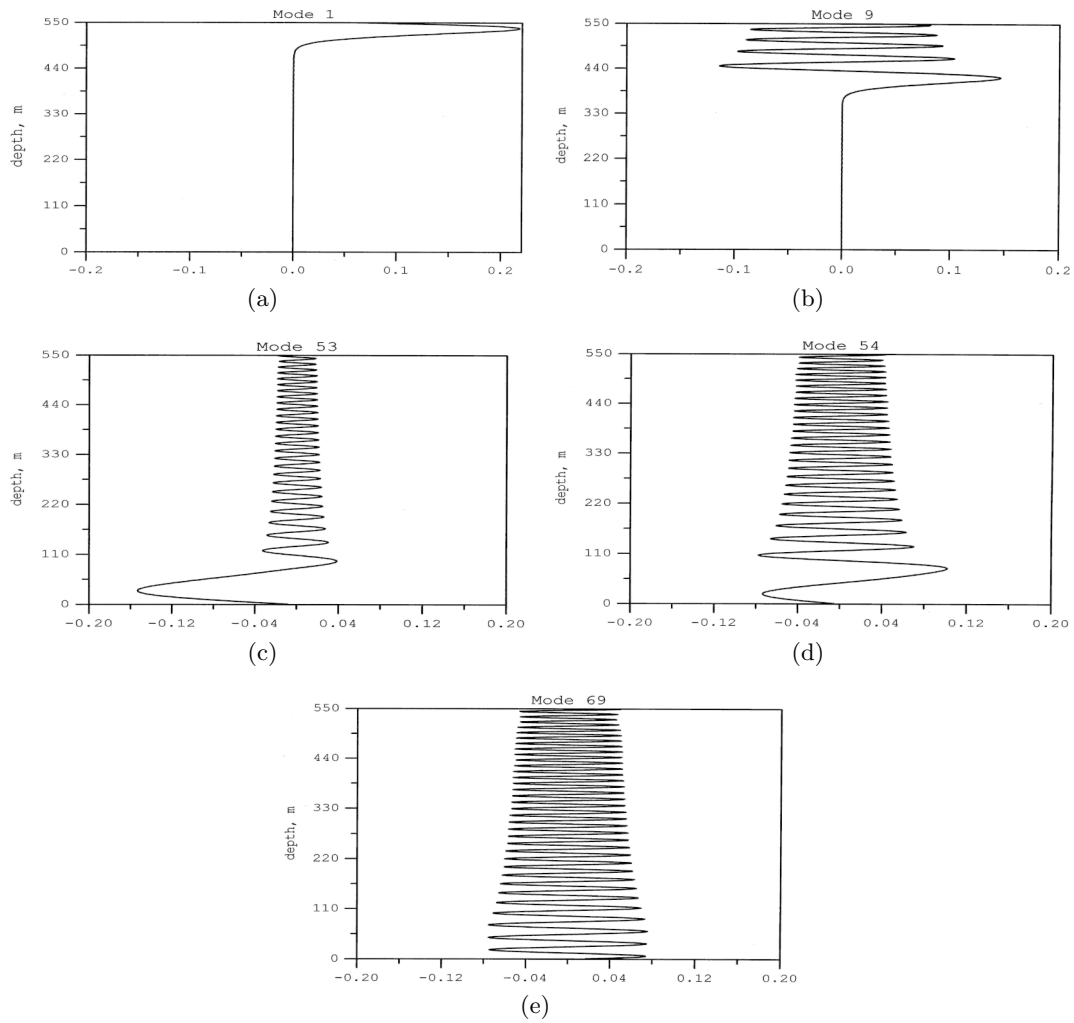


Fig. 6. Vertical mode structure for the double-duct waveguide at 460 Hz for: (a) mode 1, (b) mode 9, (c) mode 53, (d) mode 54, (e) mode 69.

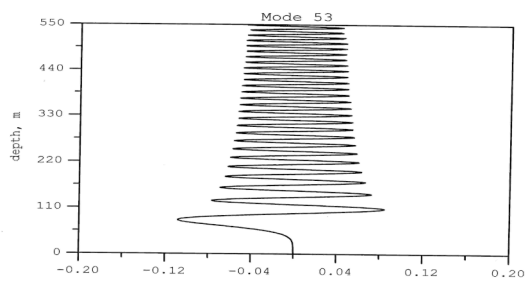


Fig. 7. Vertical mode structure for the bottom-duct waveguide at 460 Hz for mode 53.

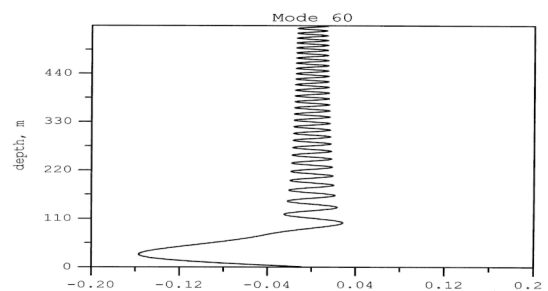


Fig. 8. Vertical mode structure for the double-duct waveguide at 526 Hz for mode 60.

Color plots of the received pressure amplitude versus depth and time at a fixed range are the informative representation of propagating pulse structure. This information is also available from experiments by using vertical arrays and time domain records. In this representation the important acoustically observable parameters are the absolute and relative arrival times of the energy packages distributed through the water-column by the waveguide

influence at a given range. The arrival times of different energy packages are commonly used by tomographical inverse techniques for the extraction of ocean properties [5]. It is important to connect the different arrival times observed in the results in Figures 3 and 4 with the waveguide characteristics responsible for energy transport rates. An excellent empirical description of the arrival path identification in the experimental data based on the modal shapes

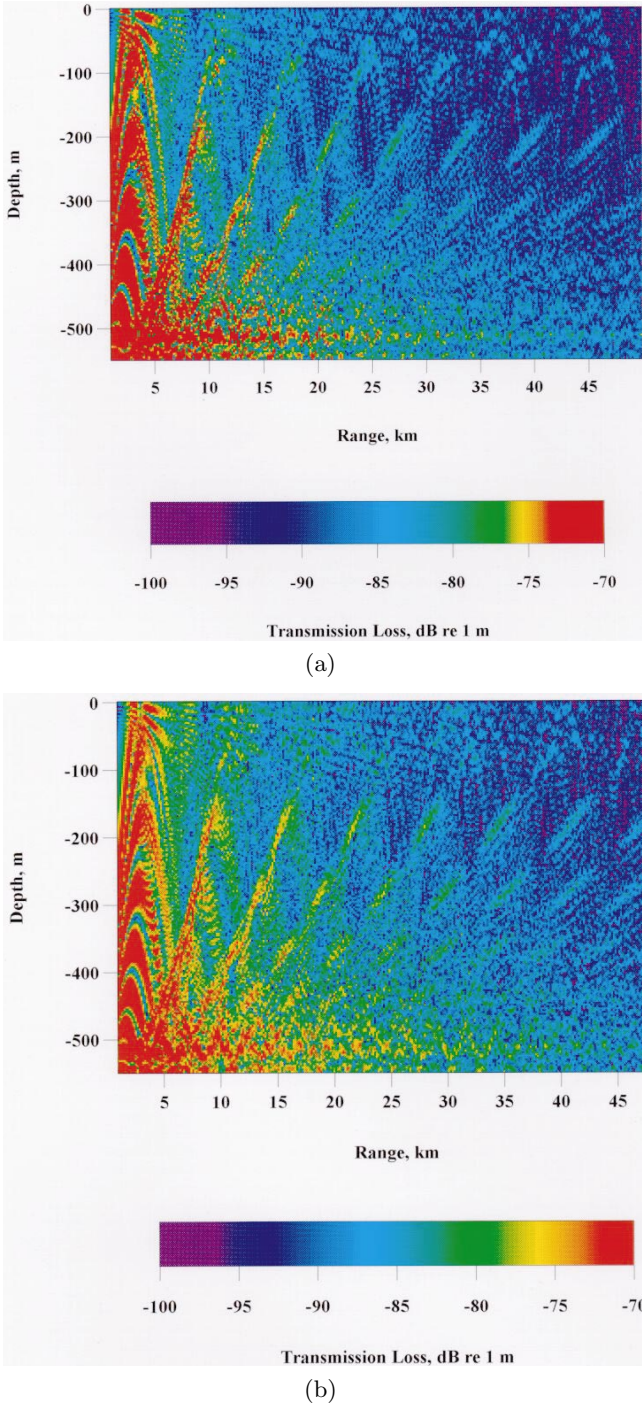


Fig. 9. Transmission losses versus depth and range for the double-duct waveguide at: (a) 460 Hz, (b) 526 Hz.

and dispersion curves for the range-independent case is presented in the referenced papers by Monjo and DeFerrari [9, 10]. In the next subsections the procedures relating the observable experimental parameters to the particular waveguide characteristics, based on the modal representation of a pulse response in a waveguide, is presented. This methodology gives the proper interpretation of the numerical results and essential to have a good grasp of

the physics of the phenomena observed in double-ducted environments.

4.1 Pulse field of an individual normal mode. Group velocity

Returning to the pulse representation at a particular spatial point in terms of normal modes, equations (16, 17) and making a reasonable assumption that $S(w)\psi_m$ is a relatively slowly varying function in comparison with the exponential term, one can assume that the oscillations of the integrand in (17) will cancel each other upon integration, except in the region near *stationary values* of the exponent with respect to the variable w . This means that integral (17) can be evaluated by means of the *method of steepest descent* [16, 20, 21]. Briefly summarizing this approach, we can rewrite the expression in the exponent in the form:

$$k_{rm}(w)r - wt = \gamma\theta(w), \quad \gamma = r, \quad \theta(w) = \left(k_{rm}(w) - \frac{wt}{r} \right). \quad (29)$$

Then, the *point of stationary phase* is given by the equation:

$$\frac{d\theta}{dw} = 0, \quad \text{or} \quad \frac{t}{r} = k'_{rm}(w_s) = \left. \frac{dk_{rm}}{dw} \right|_{w=w_s}. \quad (30)$$

Expanding the exponent in (17) into the Taylor series near the stationary phase point and limiting to the second order terms, one can arrive at the first approximation of the method of steepest descent [20]:

$$\Phi_m(r, z, t) = \frac{1}{r} \sqrt{\frac{\pi}{2|k''_{rm}(w_s)|}} \psi_m(w_s) S(w_s) \times e^{i(k_{rm}(w_s)r - w_s t \pm \pi/4)} + c.c., \quad (31)$$

where the sign in front of $\pi/4$ in the exponent term has to be the same as the sign of $k''_{rm}(w_s)$. Φ_m represents a wave process with a continuously changing-in-time phase (or frequency) through the exponential term. In accordance with definition (18), we have obtained the *frequency (or phase) modulated* pulse response for the second-order approximation. For given range r and time t , the frequency of this wave is equal to w_s . Thus, expression (30) states that the velocity with which energy travels, i.e., the *group velocity* u_m , is equal to:

$$u_m(w) = \frac{r}{t} = \left(\frac{dk_{rm}}{dw} \right)^{-1}. \quad (32)$$

The group velocity was first introduced and discussed by Lord Rayleigh in the simple context of two harmonic wave trains propagating at slightly different frequencies [22]. The group velocity is a function of the mode number and frequency in the waveguide, but it is always confined to a finite interval with both largest and smallest values of the group velocity determined by the modal discrete spectrum and the frequency band of interest. Hence,

the pulse in (16) will spread out in space and time as r increases. Analyzing (31), we can conclude that the amplitude of the pulse field of the individual normal mode Φ_m at a given time is proportional not only to the modal function $\psi_m(w_s)$ and signal spectrum $S(w_s)$, but also to the quantity $1/\sqrt{|k''_{rm}|} \propto u_m(w_s)/\sqrt{u'_m(w_s)}$. Consequently, the amplitude of the response becomes infinite when the group velocity reaches a minimum or a maximum. The theory based on the second order approximation becomes invalid in the description of the received amplitude for the corresponding frequency and time and for nearby values.

It has been shown that introducing the surface duct dramatically changes the curves of the group velocity and that the modes trapped in the surface duct have maxima in their group velocities-verses-frequency graphs that indicates the existence of precursors [9, 10]. It rises the question of how to describe the amplitudes and arrival times of precursors in analytical form. It seems that in this case one can usually follow the same type of procedure with a sufficient degree of accuracy by including the third order terms in the Taylor expansion near the stationary value. However, it is no longer assumed that the phase is exactly stationary, so the Taylor expansion now has to be done near the value w_0 , for which

$$\frac{d^2 k_{rm}}{dw^2} = 0. \quad (33)$$

Therefore, equation (29) can be expanded as:

$$r\theta(w) = r\theta(w_0) + a(w - w_0) + b(w - w_0)^3 + \dots, \\ \text{with } a = t - r \frac{dk_{rm}}{dw} \Big|_{w=w_0}, b = -\frac{1}{6} r \frac{d^3 k_{rm}}{dw^3} \Big|_{w=w_0}. \quad (34)$$

Then, the pulse field of the individual mode is [16]:

$$\Phi_m(r, z, t) = \frac{1}{2\sqrt{r}} \psi_m(w_0) S(w_0) e^{i(k_{rm}(w_0)r - w_0 t \pm \pi/4)} \\ \times \int_{-\infty}^{\infty} e^{i(a\xi - b\xi^2)} d\xi + c.c., \quad \xi = w - w_0. \quad (35)$$

Equation (35) describes an *amplitude-modulated* wave with amplitude changing in time. It means the amplitude shape of the precursors differs from the amplitude shape of the energy package trapped in the bottom duct. The integral in equation (35) can be reduced to the Airy integral [23] by changing variables, $\xi = (-\frac{1}{3b})^{1/3} y$, so expression (35) can be written as:

$$\Phi_m(r, z, t) = \frac{1}{\sqrt{r}} \psi_m(w_0) S(w_0) e^{i(k_{rm}(w_0)r - w_0 t \pm \pi/4)} \\ \times \left(-\frac{1}{3b}\right)^{1/3} 2\sqrt{\pi} v(\tau) + c.c., \quad \tau = \frac{-a}{(3b)^{1/3}},$$

where $v(\tau)$ is the Airy function which can be expressed in terms of cylindrical Bessel functions J (or modified Bessel

functions I) of order $1/3$ in the following way [23]:

$$\tau > 0, \quad \omega = \frac{2}{3}\tau^{3/2}, \\ v(\tau) = \frac{1}{3}(\pi\tau)^{1/2} [I_{-1/3}(\omega) - I_{1/3}(\omega)]; \\ \tau < 0, \quad \omega = \frac{2}{3}(-\tau)^{3/2}, \\ v(\tau) = \frac{1}{3}(-\pi\tau)^{1/2} [J_{-1/3}(\omega) + J_{1/3}(\omega)]. \quad (36)$$

Representation (36) has a number of important properties. It defines a wave packet with a pronounced amplitude maximum near $\tau = -1.02$. Thus, the stationary values of the group velocity predict conspicuous large-amplitude wave groups. Since $b \propto r$, the law of decay for the maximum of the ‘‘Airy wave’’ will be $\propto r^{-5/6}$ instead of $1/r$, which is valid for the remaining parts of the pulse as follows from (31). Therefore, as pulse travels outward from the source, the relative strength of the amplitude-modulated precursor (if we have a maximum in the group velocity) or a tail, i.e., coda, (if we have a minimum in the group velocity) will increase with range. This provides the possibility of observing the effect at long distances from a source. Figures 3 and 4 show that precursors at 42 km are observed as well as at 20 km relative to the pulse amplitude in the main peak.

It is important to mention that, strictly mathematically, arrival times of the precursor energy can not be characterized by the group velocity of the maximum. One way to obtain the arrival time of the energy maximum in a precursor can be obtained from the analysis of the argument of the Airy function which should be a subject for the future studies. Despite this firm mathematical conclusion, the arrival time of the precursors can be estimated fairly accurately by means of the group velocity, as shown below. The discussion can not leave any researcher satisfied in the sense that we still need to elaborate some general method for predicting the energy arrival times for the cases when the concept of group velocity fails. Not much has been done in this area except some very preliminary theoretical discussions without going into the details of the particular model. Much investigation is needed in this area in the future. Nevertheless, it is important to highlight some of the thoughts to complete the previous discussion and to outline a possible plan for future research.

4.2 Rate of energy transport

The other way to predict the precursor arrival time could be based on the theory of rate of energy transport. Let us start from the basic statement that the scalar wave equation represents Lagrange’s equation of motion derived from Hamilton’s Principle of classical dynamics [22]. From the Lagrange density function for a compressible nonviscous fluid, the local potential and kinetic energy densities, v and ς , can be introduced:

$$v = \frac{1}{2}\rho c^2 (\nabla^2 \Phi)^2, \quad \varsigma = \frac{1}{2}\rho \left(\nabla \frac{\partial \Phi}{\partial t} \right)^2, \quad (37)$$

where Φ is a displacement potential, ρ is the material density. Then, the rate of change of the total energy E contained in some volume V is:

$$\frac{\partial E}{\partial t} = \int_V \frac{\partial e}{\partial t} dv = - \int_S f \cdot ds, \quad e = v + \zeta, \quad (38)$$

where f is the energy flux density. For harmonic time dependence, it can be shown that the *time-averaged energy flux density* is given by [24]:

$$\bar{f} = \frac{i}{4w\rho} [p(r, w)\nabla p^*(r, w) - c.c.] = \frac{i\rho w^3}{4} (\Phi\nabla\Phi^* - c.c.). \quad (39)$$

The basic definitions allow the introduction of the *rate of energy transport* in a particular direction by mode m at a particular frequency, which can be defined for the r -direction as the ratio of the mean energy flux, \bar{F} , through a vertical section $r = \text{constant}$, to the mean energy, \bar{E} , between two such planes one r -wavelength, $\frac{2\pi}{k_{rm}}$, apart [25]:

$$\nu_m = \frac{\bar{F}}{\bar{E}}, \quad \bar{F} = \int (\bar{f})_r dz, \quad (40)$$

where $(\bar{f})_r$ denotes the r -component of the energy flux density.

This concept is effective when dealing with normal mode solutions. The displacement potential can be represented as:

$$\Phi_m = c_m U_m(z) R_m(r), \quad \text{where } R_m(r) = \sqrt{\frac{2}{\pi k_{rm} r}} e^{ik_{rm} r}.$$

The index m referring to the particular mode m will be omitted below. Using the Helmholtz equation, one has for the potential energy:

$$\Pi = \int_V v dv = \frac{1}{2} \int_V \frac{w^4}{c^2} \rho \Phi^2 dv. \quad (41)$$

The total kinetic energy T in the volume V for normal mode representation can be given after some mathematical manipulations as

$$T = \int_V \varsigma dv = \frac{1}{2} \int_V \frac{w^2}{c^2} \rho \left(\frac{\partial \Phi}{\partial t} \right)^2 dv. \quad (42)$$

For a harmonic wave $T = \Pi$, and

$$\bar{E} = 2\bar{T} = \frac{k_{rm}}{2\pi} \int_0^{2\pi/k_{rm}} dr \int_0^\infty \frac{w^4}{c^2} \rho \Phi^2 dz. \quad (43)$$

Substituting (43) in (40), we arrive at:

$$\nu_m \approx \frac{k_{rm}}{w} \frac{\int_0^\infty \rho U_m^2(z) dz}{\int_0^\infty \frac{\rho}{(c(z))^2} U_m^2(z) dz}, \quad (44)$$

where $U_m(z)$ is a vertical modal function for an arbitrary sound speed profile. As an advantage, SWAMP allows one to obtain ν_m in terms of integrable analytical functions. (Refer to Sect. 3.1) The numerical comparison between the rate of energy transport, determined by (44), and the conventional concept of group velocity will be left for future study.

4.3 Relationships between acoustic and environmental parameters

Returning to the basic experimental model and using the definition of group velocity, an approximate time for mode m to travel between two points r_0 and r_1 ($r_0 < r_1$) in range can be estimated as:

$$t_m^r = \frac{r_1 - r_0}{u_m^r}, \quad (45)$$

where t_m^r is the arrival time at the particular range point determined by the group velocity u_m^r . We can introduce an average velocity, the “vertical mean group velocity”, which characterizes the mean time necessary for the energy carried by mode m , with modal angle θ_m , to propagate between two vertical points:

$$u_m^z = \sqrt{c_{av}^2 - (u_m^r)^2}, \quad (46)$$

where c_{av}^2 is the mean sound speed in the bottom duct. The time it takes to go from z_0 to z_1 is:

$$t_m^z = \frac{z_1 - z_0}{u_m^z} \approx \frac{d}{u_m^z}, \quad (47)$$

where d is the average depth separation between the source and the surface duct. Then the first bounce of mode m in the surface duct is determined in time and range as follows:

$$t_1 = \frac{d}{u_m^z} \text{ at } r_1 = \frac{d}{\tan \theta_m}, \quad (48)$$

where θ_m is the modal angle measured relative to the horizontal axis.

A reasonable assumption is that only high order modes (with high modal angle) can make it to the surface, because the low-order modes are trapped in the wide bottom duct for a source near bottom. Hence, the high modal angle θ_m can be approximated by the critical angle, which is, in a crude approximation,

$$\theta_m \approx \theta_{cr} \approx \cos^{-1}(c_{av}/c_b), \quad (49)$$

where c_b is the sound speed in the bottom half-space. (For the basic model $\theta_{cr} \approx 13.5^\circ$.) After the first bounce, part of the energy carried by high-order modes becomes trapped in the surface duct and travels through the surface duct to the receiver at range r_1 . It determines the arrival time for the first precursor. Much of the energy leaks back to the bottom with the modes which are only partially

trapped in the surface duct and arrives back at the surface duct after reflection from the bottom. The time to the second bounce can be approximated by:

$$t_2 = \frac{3d}{u_m^z} \text{ at } r_2 = \frac{3d}{\tan \theta_m}. \quad (50)$$

The fact that the source is placed very close to the bottom has been used to simplify formula (50). Proceeding in this manner, one can estimate the arrival times of the different precursors at a given range r_1 :

$$\begin{aligned} t_I &= \frac{d}{u_m^z} + \left(r_1 - \frac{d}{\tan \theta_m} \frac{1}{u_{\max}^r} \right), \\ t_{II} &= \frac{3d}{u_m^z} + \left(r_1 - \frac{3d}{\tan \theta_m} \frac{1}{u_{\max}^r} \right), \\ t_{III} &= \frac{5d}{u_m^z} + \left(r_1 - \frac{5d}{\tan \theta_m} \frac{1}{u_{\max}^r} \right), \\ &\dots, \\ t_n &= \frac{(2n-1)d}{u_m^z} + \left(r_1 - \frac{(2n-1)d}{\tan \theta_m} \frac{1}{u_{\max}^r} \right), \end{aligned} \quad (51)$$

where u_{\max}^r is the maximum group velocity of mode m characterizing the propagation in the surface duct. The lag time between the arrivals of two adjacent precursors is equal to:

$$\begin{aligned} \Delta t &= \frac{2d}{u_m^z} - \frac{2d}{\tan \theta_{cr}} \frac{1}{u_{\max}^r} \\ &= 2d \left(\frac{1}{\sqrt{c_{av}^2 - u_{rm}^2}} - \frac{1}{\tan \theta_{cr}} \frac{1}{u_{\max}^r} \right) \\ &\approx 2d \left(\frac{1}{c_{av} \sin \theta_{cr}} - \frac{\cos \theta_{cr}}{u_{\max}^r \sin \theta_{cr}} \right) \\ &\approx \frac{2d}{c_{av} \sin \theta_{cr}} \left(1 - \frac{c_{av}}{u_{\max}^r} \cos \theta_{cr} \right). \end{aligned} \quad (52)$$

The Florida Straights environment can be characterized by $c_{av} = 1517.5$ m/s and $u_{\max}^r \approx 1544.5$ m/s, which is the average sound speed in the surface duct. For $d = 550$ m, the arrival time of the first precursor is estimated to be 27.26 seconds at 42 km. Expression (52) gives a lag time of 0.1 seconds which is in a good agreement with the numerical and experimental results. (Refer to Figs. 3 and 1a.) Equations (51, 52) show that both the bottom properties and the surface duct parameters are involved in the determination of the arrival times and the temporal spacing between precursors. Ray theory would indicate that only duct characteristics are responsible for the arrival times of the precursors, which is generally not true. In addition, one has to be very careful with using ray models to investigate this effect. It has been concluded that the standard ray models do not give an adequate picture of the effect. (More details are in [9,10].)

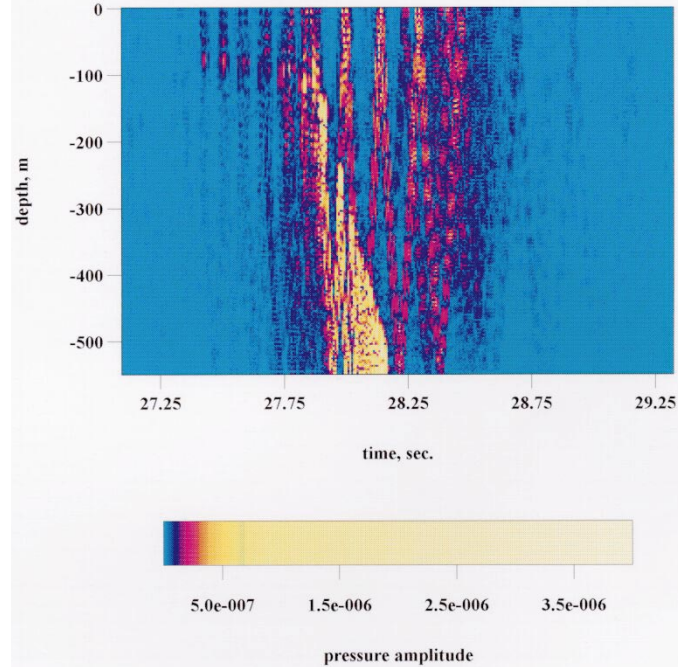


Fig. 10. Pulse response at 42 km for wide surface duct.

Figure 10 shows the pulse response at 42 km when the sound speed varies in the surface duct from 1530 m/s at the surface to 1541.5 at 100 m, so that we have a wider surface duct than in the basic model. The gradient of the sound speed change in the surface duct becomes the same as in the bottom duct. I shall refer to this input model as “wide duct case”. The simulations show that the lag time between precursors decreases and the precursors are wider. The arrival time of the first precursor is delayed, which is generally understandable from the decreased average sound speed in the surface duct.

The numerical results in Figures 11 and 12 are based on the parameters of the basic model for the water column, but the speed in the bottom is 1690 m/s. The pulse responses are calculated at 30 and 20 km ranges. One can see that the bottom influence on precursor structure is not very pronounced, but it produces noticeable changes in the tail of the pulse, making it “ring” much longer, so that the time window (2.2 seconds) used in the calculations does not allow getting adequate color maps at 42 km because of the wrap-around effect of the Fast Fourier Transform. The pulse “ringing” time increases because the critical angle is higher, so that the source generates more high-order modes. They can travel through the entire water column and be classified as Multiple Surface-Reflected-Bottom-Reflected (MSRBR) paths by analogy with a ray picture. The arrival times for high-order modes (not trapped in the surface duct!) are functions of the path length, so high-order modes arrive after low-order modes trapped in the bottom duct. Figure 11 for the range of 30 km shows very clearly that the MSRBR paths do not manifest themselves with a constant time lag for the fixed depth. It confirms again that the equally-spaced-in-time-precursors cannot be associated with any type of MSRBR energy arrivals.

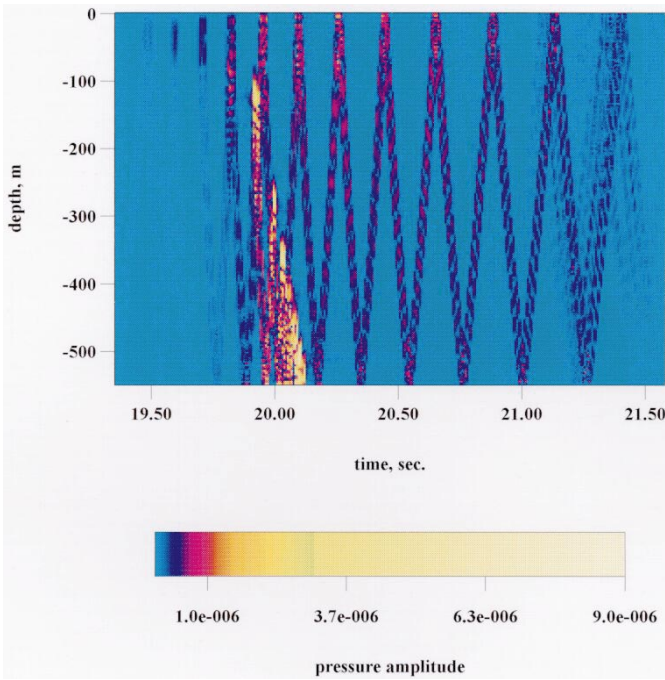


Fig. 11. Pulse response at 30 km for fast bottom.

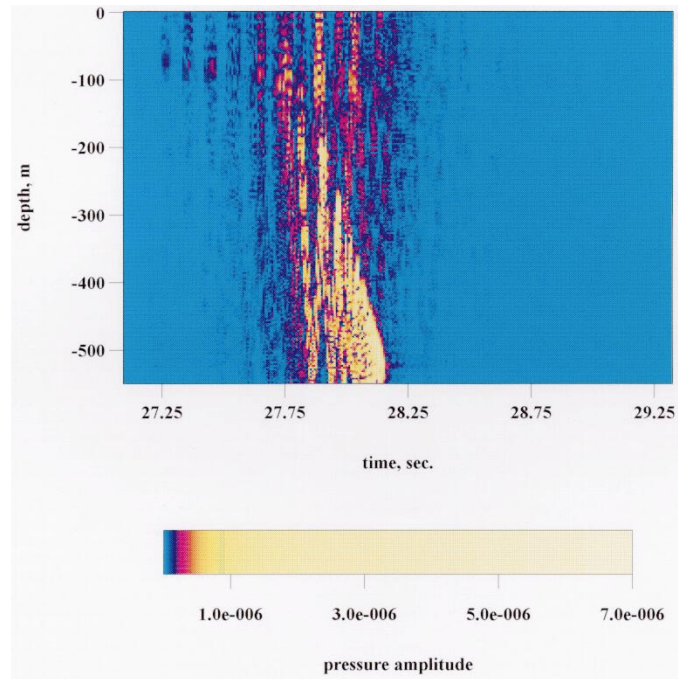


Fig. 13. Pulse response at 42 km for low density bottom.

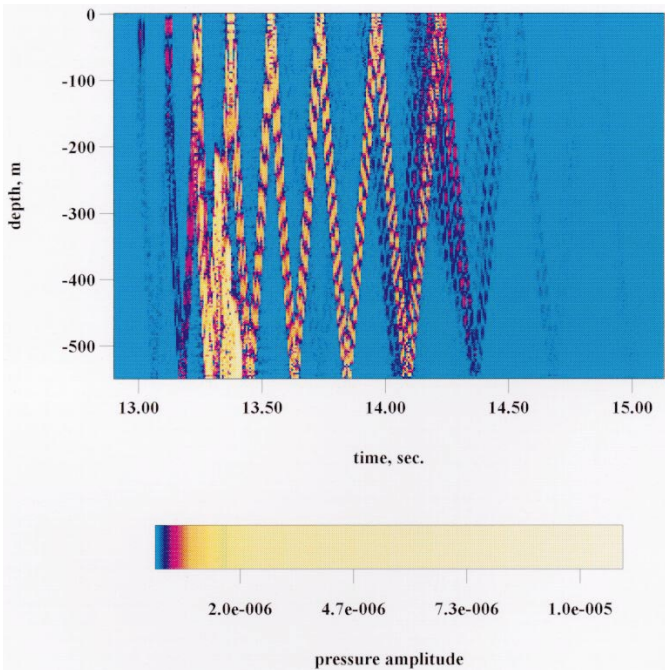


Fig. 12. Pulse response at 20 km for fast bottom.

It might occur in this context that a few MSRBR energy packages could arrive faster than the main energy package, if they were more a function of the sampling of the complete sound speed profile than a function of the path length. Figure 13 demonstrates the pulse response for the wide surface duct case with a lower density ($\rho = 1.2 \text{ g/cm}^3$) in the bottom. Once again the bottom does not visibly influence the precursor arrivals, and, in addition, the density parameter plays much less of a role

in the formation of the pulse tail shape than the sound speed in the bottom layers. All of the demonstrated numerical results allow one to formulate the conditions for which the effect can be observed. The most pronounced precursors exist for a narrow surface duct. Hence, we can talk about the better focusing quality of a narrow surface duct despite its weaker gradient. The probable reason is that the width of the duct is an effective parameter for filtering the interval of modal angles which are trapped in the surface duct. The smaller the angle interval trapped in the duct is, the more narrow the time response for the particular precursor is, because the difference in the energy transfer rate within the narrow angular interval of modal angles is small.

Figure 14 shows the pulse response at 42 km for the basic set of parameters, when the source is in the surface duct at a depth of 30 m. The first energy packet arrives at approximately 27.2 seconds. It is 0.05 seconds earlier than for the case with the source in the bottom duct (compare to Fig. 3). This is the time which is needed by the high-order modes to transport energy into the surface duct where it gets trapped. (Refer to the first equation in formulae set (51).) Then the remainder of the energy goes the same way. Part of the energy is carried by the surface duct trapped modes to the receiver directly through the surface duct. The other part of the energy leaks to the bottom with the leaky modes as in Figure 6d. Reflected from a bottom, energy comes back to the surface, becomes partially trapped and travels near the surface, forming the second precursor arrival. The delay between arrival times of the individual precursors is the same as for the near-bottom-source as would be expected. From a theoretical point of view, changes in the source depth do not change the environmental parameters, consequently,

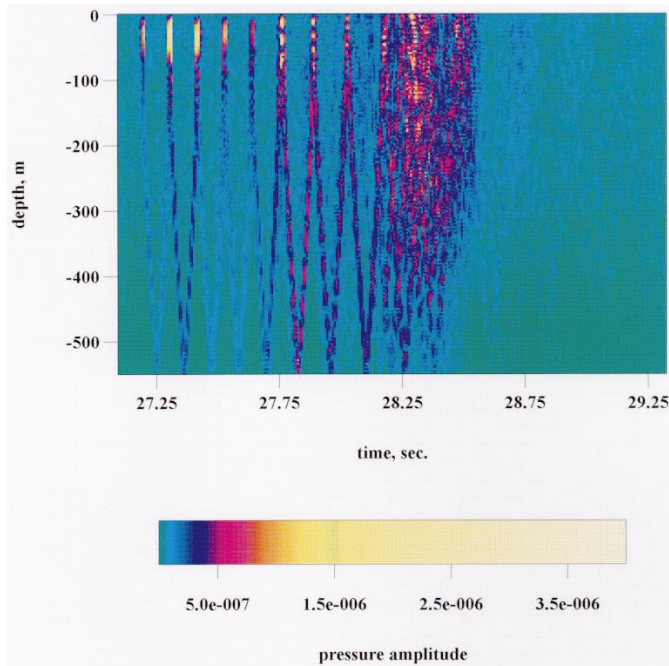


Fig. 14. Pulse response at 42 km for the source in the surface duct.

they do not change the vertical modal structure. Hence, the same spectrum of modes is generated. Recall that the individual mode field in equation (15) is proportional to the product of the vertical modal eigenfunction and its excitation coefficient, which is the value of the eigenfunction at the source depth: $\psi_m(z, z_s, w, \lambda_m) \propto U_m(z_s)U_m(z)$. At this point it is apparent that moving a source changes the excitation coefficients of the modes. The high-order modes are enhanced and the low-order modes, which have small amplitudes near the surface (as is shown in Figs. 6a, b), are suppressed by placing a source in the surface duct. This causes the absence of energy trapped in the bottom duct in Figure 14. This may result in the problem of the separation of the precursors and the MSRBR energy arrivals, because the bottom trapped energy, played a natural boundary role between those two in the previous figures, is not seen. At this point, let us discuss the necessary conditions for the existence of the precursors. The primary condition is the presence of a double ducted environment. The numerical results have shown that the requirements on the parameters of surface ducts are not strict. This makes the effect easily observed as long as double ducting exists.

The next most sensitive parameter is the frequency band. Figure 15 shows the basic model pulse response versus depth and time at ranges of 42 km for a carrier frequency of 100 Hz. There are no precursors in the frequency band of 75–125 Hz. To understand a reason, one should analyze the dependence of the vertical modal structure on frequency for the modes, which can be potentially trapped in the surface duct. The results show that the high-order surface grazing modes associated with trapping in the surface duct have the lowest cut-off frequencies higher than

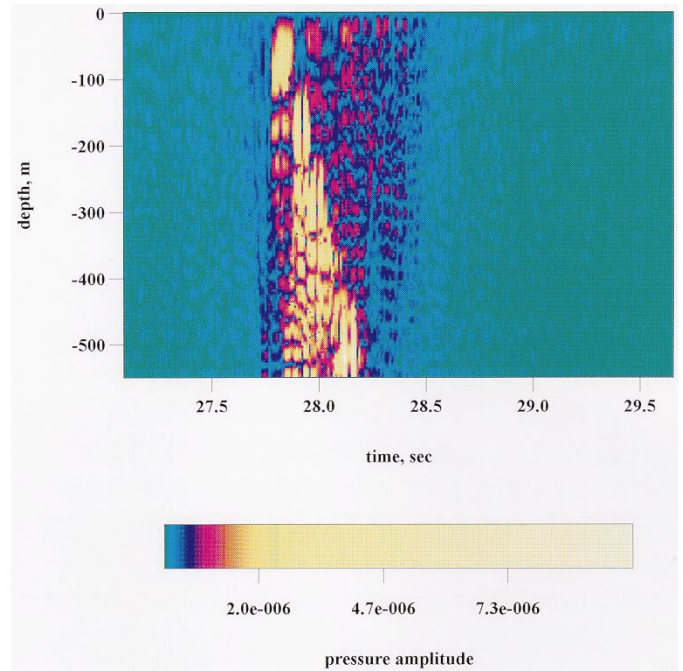


Fig. 15. Pulse response at 42 km for the central frequency of 100 Hz.

the given frequency band. Due to this fact, the “precursor effect” can not be observed for this frequency band. Consequently, the “precursor effect” can be referred to as a high frequency effect. Sufficiently high-frequency broadband pulse must be generated to observe precursors.

The propagation model considered above can be referred to as a deep-water propagation model. There is no strict definition allowing the distinction between shallow- and deep-water propagation patterns. A reasonable factor to characterize the specific features of these two cases could be the relation between the water-column depth, h , and the propagating signal wavelength, λ . Usually, cases of $kh < 10$, $k = \frac{2\pi}{\lambda}$, are typical in coastal or continental shelf waters, i.e., in shallow water propagation scenarios one deals mostly with kh less than 10. But we always should keep in mind that the use of very high frequency in coastal waters leads to conditions similar to deep water ones. The modern experimental trend is to study acoustical propagation in shallow water, such as encountered in some regions of interest in the Yellow, Mediterranean Seas, or Hawaii Pacific region. These environments are characterized by more shallow waters, ~ 80 m, but still have the seasonal presence of the weak surface duct in addition to very wide, gradual bottom ducts. From the applied point of view, it would be important to test how the described phenomenon manifests itself in shallow water. The results of numerical modeling for the environmental conditions encountered in the Yellow Sea are discussed in Section 5. Before going to the next section, let us briefly summarize how the information about the parameters characterizing the source localization, bottom properties, and sound speed profile that are of the interest of the inverse problem solution can be inferred.

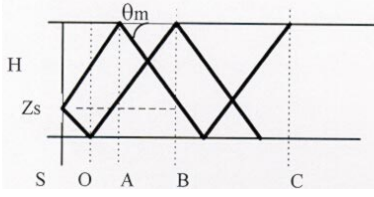


Fig. 16. Mode representation as a superposition of up-going and down-going plane waves for source localization.

4.4 Extraction of source or environmental parameters from the received pulse structure

This section addresses general methodology for inferring the information about a source location and environmental integrated parameters from the measured pulse structure. More rigorous inversion techniques will be required to make an accurate estimation of a source position in real noisy ocean environment based on vertical array data. The discussion of these techniques lays out of the scope of the paper.

Let us refer to the faster bottom case, namely to Figure 11, where the separation between high-order and low-order modes is most apparent.

- (a) *Source localization.* Let us consider the high-order mode group arrival times at a fixed depth as schematically shown in Figure 16. The particular high-order mode which is not trapped in the surface duct (it belongs to the “tail” of the pulse) or the cluster of modes with the same modal angle (for pulse signals) can be represented as a pair of up-going and down-going plane waves. Then, the time lags between the two closest and two next closest arrivals, Δt_{AB} and Δt_{AC} , can be converted to range by using the concept of group velocity u_m for this modal cluster:

$$\begin{aligned} r_{AB} &= u_m \times \Delta t_{AB}, \\ r_{AC} &= u_m \times \Delta t_{AC}. \end{aligned}$$

A simple chain of geometric manipulations can be worked out to obtain the vertical source localization:

$$\begin{aligned} r_{AB} &= r_{SO} + r_{OB} - r_{SA} = (H - z_s) \cot \theta_m + H \cot \theta_m \\ &\quad - z_s \cot \theta_m = 2(H - z_s) \cot \theta_m = 2(H - z_s) \frac{r_{AC}}{2H}, \\ \Rightarrow \Delta t_{AB} &= \Delta t_{AC} \frac{r_{AB}}{r_{AC}} = \Delta t_{AC} \left(1 - \frac{z_s}{H}\right). \end{aligned}$$

We arrive at the localization expression:

$$z_s = H \left(1 - \frac{\Delta t_{AB}}{\Delta t_{AC}}\right). \quad (53)$$

Hence, the only environmental information required for the estimation of the vertical position of a source in range-independent waveguides is the depth of a water column. The time delays in the last formula can be extracted from measured data subject to the required experimental setup. When the source is very close to the bottom, Δt_{AB} is very small. This is the case for

Figure 11, where $\Delta t_{AB} \approx 0.028$ s. is practically determined by the width of the line of the energy front. When a source is very close to the surface, the difference between the time lags is also very small. These two cases are very difficult to distinguish because the energy fronts intersect in the source and its “image” vertical location. Therefore, some other information about pulse energy distribution must be utilized to make decisions in these cases.

It is important to notice that usually precursors do not contain evident information about the vertical source localization. Only, if the source is at the middle of water column, one can identify the difference in lag times between the first two and between later ones. Thus, one can associate the first temporal lag with source location. On the other hand, all next time lags will be related to the depth of water column (see Eq. (52)). If one has a priori information about environment and if the vertical coordinate of a source is estimated, then the arrival time of the first precursor can be used to estimate the source range. (Refer to Eq. (51).)

- (b) *Bottom critical angle.* From the analysis of the inclination angles of energy front curves, one can conclude that the energy front of the low-order mode group, trapped in the bottom duct, forms a ninety degree angle with the horizontal axis. The energy front is perpendicular to the propagation direction of a particular cluster of modes. If the attenuation in the bottom is not strong, then we can successfully observe the tail of the pulse, which is the case in Figure 11. The tail is formed by high-order modes, which are related to the MSRBR paths. The inclination angle of energy fronts arriving at a particular range gradually changes over time from ninety degrees to the angle ϑ (with the horizontal direction), which is directly related to the critical angle, as $\theta_{cr} = 90^\circ - \vartheta$. The estimated critical angle will provide the information only about integrated bottom properties.

This discussion shows that if one has detailed vertical structure of a pulse recorded by the vertical array spanning a water column, then the crude estimation of source position and environmental parameters can be made.

5 Numerical simulation of pulse propagation in the shallow-water yellow sea environment

Typical Yellow Sea sound speed profile has a much stronger gradient as is shown in Figure 17. The proposed Yellow Sea Test Areas have a muddy-sand type of bottom, which is relatively fast. The bottom characteristics for modeling have been left the same as for the Florida Straits because of the lack of descriptive experimentally measured bottom parameters. In presented calculations a weak surface duct in the first ten meters of water occurs. Shallow-water measurements require higher frequencies and wider frequency bands to achieve a resolution comparable to the deep-water cases. The reason is that mode stripping due to strong bottom interaction is more pronounced in range

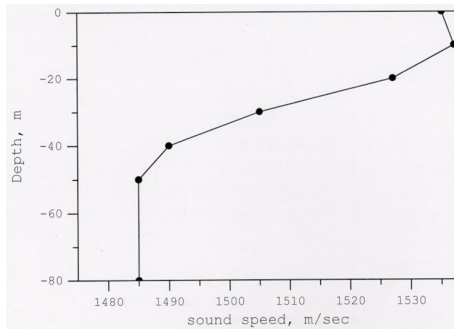


Fig. 17. Representative sound speed profile for shallow Yellow Sea waters.

for shallow water and may lead to vague results in range as more and more modes are stripped, particularly, when the number of generated modes is small. In modeling a source has been placed at the depth of 60 m in the bottom duct.

Figure 18 shows color maps of the transmission loss versus range and depth for the frequency of 2800 Hz. The trapping of low-order modes in the bottom duct and very strong stripping of high-order modes after 10 km is observed. Shallow water cases require short-range measurements because of the intensive mode interaction with the bottom. The transmission loss map over a range of 10 km in Figure 18b shows more details of energy trapping effect from high-order modes near the surface, so one can expect the formation of precursors in the pulse structure. For the pulse propagation simulations a frequency band from 2.8 kHz to 3.6 kHz, with a central (carrier) frequency of 3.2 kHz, has been used. The pulse responses at 3 and 5 km are shown in Figures 19 and 20. There are strong precursors present, leading the main bulk of arrivals at both ranges. One can also observe that the effect of the strong bottom duct is more evident. The energy outline of the bottom duct is associated with the actual sound speed profile outline to a reasonable degree of accuracy. I can speculate based on modeling that the energy distribution in the bottom duct can be converted to the sound speed profile with satisfactory accuracy by designing an inverse procedure. Strong diffraction causes the energy fronts to bend. The splitting between the up-going and down-going wave energy fronts becomes more pronounced as the source moves to the mid-point. This makes vertical source localization easier. Equal splitting occurs when the source is at the middle of the water column, as shown in equation (53). As a conclusion, it can be stated that in a shallow water environment the precursors due to a weak surface duct again appear to be very sensitive indicators of seasonal environmental parameters variations (as was also the case in the deep water channel in the Florida Straits). Very often range dependence and mode coupling take place in real ocean. A more detailed understanding of surface duct propagation requires extensive and systematic range-dependent modeling. In the next chapter some examples of range-dependent propagation are considered.

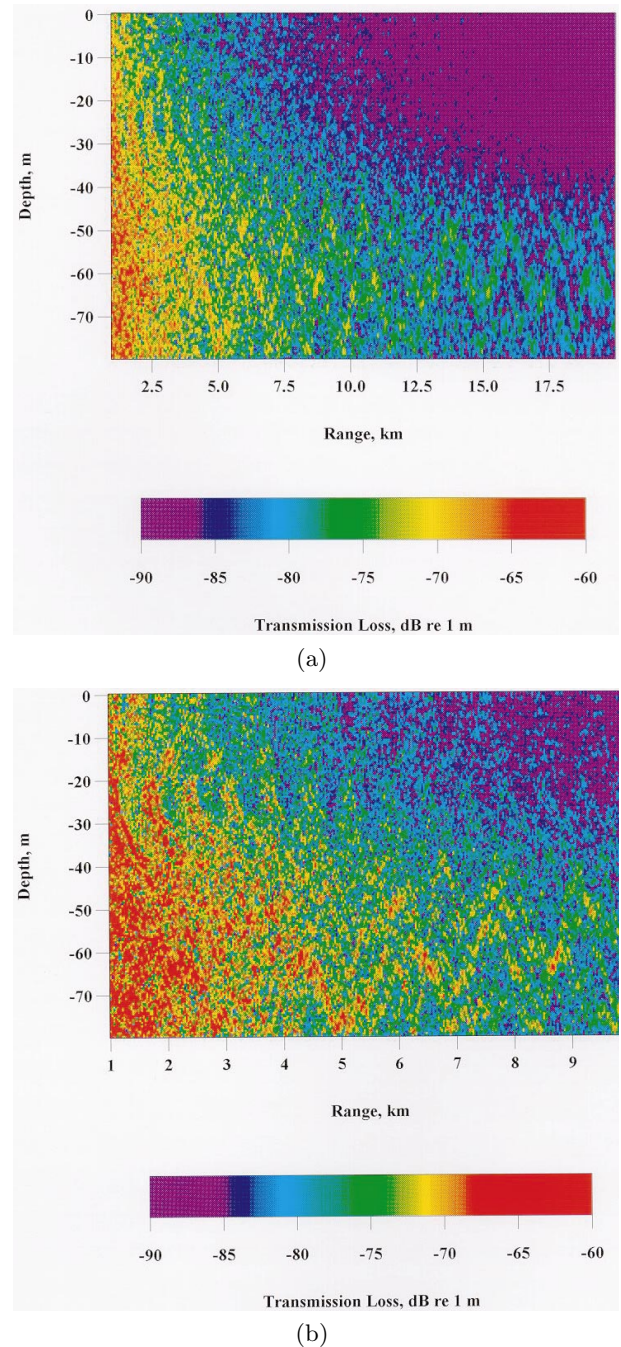


Fig. 18. Transmission losses versus depth and range for Yellow Sea environment for 2800 Hz: (a) up to 20 km in range, (b) up to 10 km in range.

6 Numerical simulation results for a range-dependent deep-water environment

A range-dependent model has all the signal and environmental parameters of the basic model except the bottom profile (bathymetry). It has a range-independent subregion up to 30 km, which is identical to the basic model. Then the water column depth changes from 550 m to

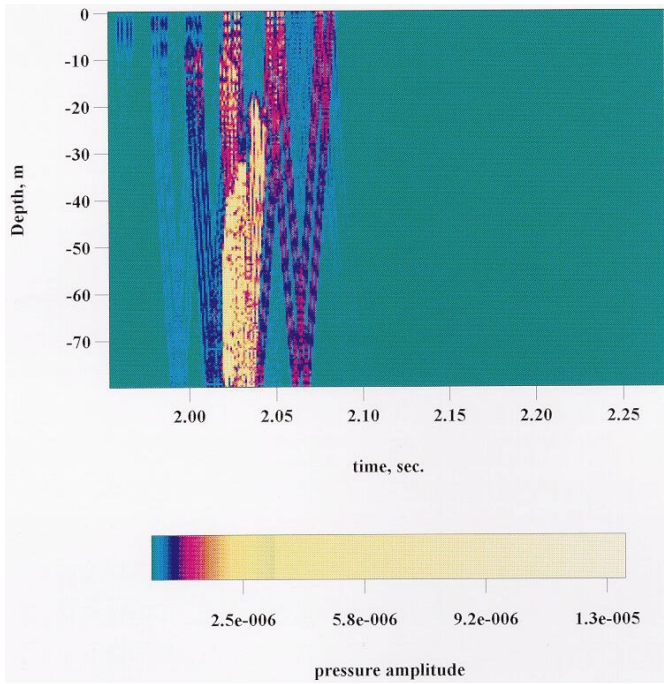


Fig. 19. Yellow Sea pulse response at the range of 3 km.

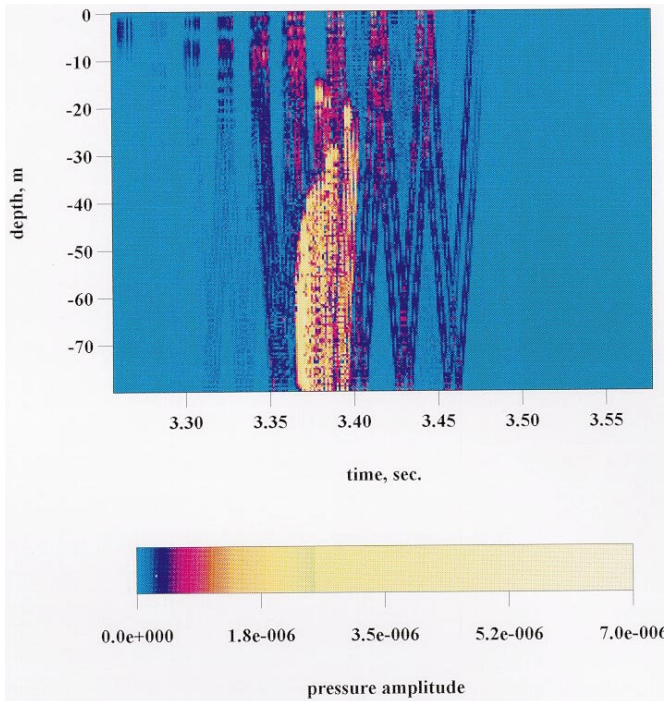


Fig. 20. Yellow Sea pulse response at the range of 5 km.

450 m over a range of 10 km. From 40 km to 50 km the water column depth is again constant and equal to 450 m. The upslope angle is 0.6 degrees, and the source is placed at depth 512 m. A color map of the transmission loss versus depth and range at 526 Hz is presented in Figure 21. It can be observed that the energy trapping in the surface duct is less effective for the range-dependent subregion in

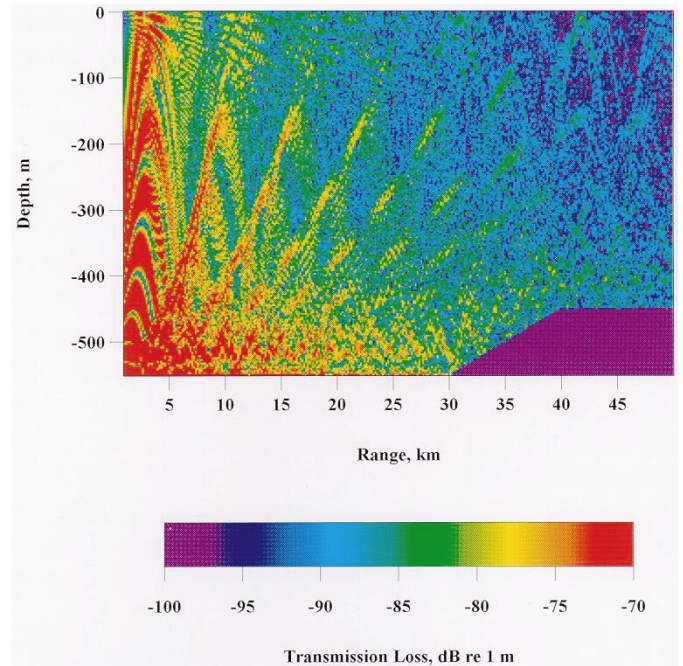


Fig. 21. Transmission losses for range dependent Florida Straits environment at 526 Hz.

comparison to the range-independent case shown in Figure 9b. The pulse response at 42 km is shown in Figure 22.

Comparing the results presented in Figure 3 (range independent bathymetry) to Figure 22 (range dependent bathymetry), one can see that the range dependent case is very different. Even a weak short-range change in bathymetry forms a completely different structure of precursors. The arrival time of the first two precursors and their vertical structure near the surface are unchanged because they are primarily formed in the range independent subregion. The fixed lag time for the rest of precursors is lost, and decreases for the later ones. The absence of a fixed temporal separation between precursors indicates the presence of range dependence in the propagation channel.

The conclusion is that the time lags between precursor energy packets decrease for up-slope problems, while they increase for down-slope problems, if the properties of the surface duct do not vary with range. With range dependence, each precursor may have just one particular path owing to leakage at one particular range. Thus, the time separation between two precursors can also vary in range. The duct loses its focusing property, so precursors are wider and less clear, especially outside the surface duct. This makes measurements of the precursors difficult at receivers placed outside the surface duct, as has been indicated in the experimental data sets for range-dependent propagation paths [9,10]. The variation of ocean properties and bathymetry in range shows that many interesting effects are possible in range. We can expect more dramatic changes in pulse structure for longer and stronger range dependencies. Much more research on this topic should be done in the future.

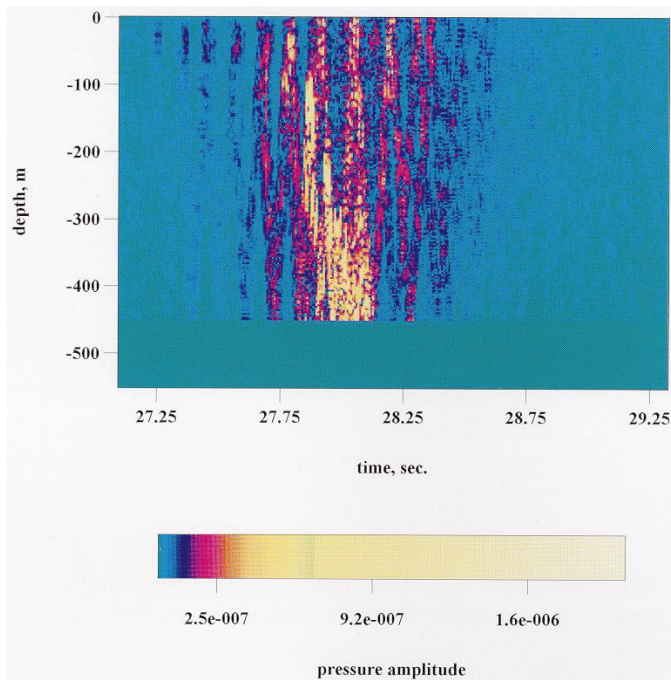


Fig. 22. Pulse response at 42 km for range dependent Florida Straits environment.

7 Conclusions

This study has focused on the problem of pulse propagation in ocean waveguides by using the numerical simulation results from the new normal mode model – SWAMP. By using the results of numerical modeling, a systematic study of pulse propagation in double-ducted environments has been achieved.

SWAMP was used for the time-domain analysis of the broadband pulse propagation in double-ducted waveguides. Several deep-water and shallow-water scenarios were examined. The phenomenon of the formation of discrete precursors in time in the presence of double ducting is very persistent for all examined environments for high enough frequencies. That illustrates the importance of the effect for double-ducted environments. The physics of the precursors is very complicated and generally based on the fact that the surface duct generates a unique series of perfectly trapped and leaky modes near the ocean surface. For range-independent problems the time separation between precursors is fixed. The temporal separation among precursors in numerical simulations is in a good agreement with experimental data. It is shown that the complete physics of precursors can not be described by the conventional concept of the group velocity, which fails due to a stationary point in the “group velocity versus frequency” curves in the presence of the surface duct. It is proposed to explain the actual physical process of energy transport on the basis of the mean rate of energy transport in terms of the mean energy flux over some unit region, divided by the mean energy in the region. The results of the numerical simulations show that the range-dependence has a strong influence on the separation in precursor arrival

times and their amplitude modulation which was also indicated in the experimental data. The presence of precursors appears to be sensitive to range dependence and may be diminished due to rapidly changing bathymetry.

The numerical results suggest a number of possibilities for extracting a source location and environmental parameters from a received pulse structure. The number of precursors can be directly translated into a source localization in range. The amplitude modulation of a particular precursor is related to the characteristics of the surface duct, namely its width and the gradient of the sound speed profile. An analysis of the arrival times of the “tail” of the pulse gives information about bottom, such as the critical angle related to the integrated bottom impedance. The difference in arrival times of the high-order modes not trapped in the surface duct can be effectively utilized for the source localization in depth. The energy distribution of the low-order modes trapped in the bottom duct can be used to obtain the gradient of the sound speed in the bottom duct. The problems of precursor behavior in the presence of scattering from objects and range dependence poses very challenging issues for future research.

This work was supported by the Office of Naval Research and the Louisiana Board of Regents Support Fund (Contract No. LEQSF(2001-04)-RD-A-38). I would like to thank Prof. H.A. DeFerrari and Dr. C.L. Monjo of the University of Miami for the initiation of the author’s involvement in these studies, for the fruitful discussions and for providing the experimental data; Dr. Michael F. Werby of Naval Research Laboratory for his great contribution in writing the original version of SWAMP; and Prof. Juliette Ioup and Prof. George Ioup of the University of New Orleans for research guidance and valuable comments on the presented studies. *My very special gratitude goes to my mother, Svetlana I. Abrossimova, for encouraging me to publish this paper.*

References

1. N.A. Sidorovskaia, M.F. Werby, Broad-band pulse signals and the characterization of shallow water ocean properties, in *Proceedings of the SPIE Conference (Orlando, Florida, USA, April 1995)*, pp. 97–108
2. N.A. Sidorovskaia, A New Numerical Technique for the Unification of Propagation and Scattering Problems in Underwater Acoustics, in *Proceedings of IMECE2001: 2001 ASME International Mechanical Engineering Congress and Exposition (New York, NY, USA, November 11-16, 2001)*
3. A.I. Khil’ko, J.W. Caruthers, N.A. Sidorovskaia, *Ocean Acoustic Tomography. A review with Emphasis on the Russian Approach* (Russian Academy of Sciences, Institute of Applied Physics, Nizhny Novgorod, 1998)
4. M.F. Werby, M.K. Broadhead, R. Field, N.A. Sidorovskaia, Determination of velocity profile and sea bed characteristics from high frequency pulse propagation in a shallow water Mediterranean environment, in *Proceedings of the Conference on High Frequency Acoustics in Shallow Water (Lerici, Italy, 1997)*

5. W. Munk, P. Worcester, C. Wunsch, *Ocean Acoustic Tomography* (Cambridge University Press, New York, 1995)
6. W. Munk, R. Spindel, A. Baggeroer, T. Birdsall, *J. Acoust. Soc. Am.* **96**, 2330 (1994)
7. P.F. Worcester, et al., *J. Acoust. Soc. Am.* **95**, 3118 (1994)
8. J.M. Schneider, N.A. Sidorovskaia, Illumination Studies for Imaging Subsalt Anomalies, in *Proceedings of Offshore Technology Conference (Houston, TX, USA, 3-6 May, 2000)*, (paper#: OTC 11983)
9. C.L. Monjo, H.A. DeFerrari, *J. Acoust. Soc. Am.* **95**, 3129 (1994)
10. C. Monjo, Analysis of pulse propagation in a bottom limited sound channel with a surface duct, Ph.D. Dissertation, University of Miami, Coral Gables, Florida, May 1993
11. N.A. Sidorovskaia, Time-domain study of acoustic pulse propagation in an ocean waveguide using a new normal mode model, Ph.D. Dissertation, University of New Orleans, May 1997
12. <http://www.ucl.ac.uk/~nxs7560>
13. J.E. Murphy, *J. Acoust. Soc. Am.* **77**, 1958 (1985)
14. B.E. McDonald, W.A. Kuperman, *J. Acoust. Soc. Am.* **81**, 1406 (1987)
15. L. Nghiem-Phu, F. Tappert, *J. Acoust. Soc. Am.* **78**, 164 (1985)
16. L.M. Brekhovskikh, *Waves in Layered Media* (Academic Press, Inc., New York, 1980)
17. W.H. Press, S.A. Teukolsky, W.T. Vetterling, B.P. Flannery, *Numerical Recipes in FORTRAN* (Cambridge University Press, New York, 1994)
18. F.B. Jensen, W.A. Kuperman, M.B. Porter, H. Schmidt, *Computational ocean acoustics, AIP series in modern acoustics and signal processing* (AIP Press, New York, 1994)
19. V.V. Varadan, Elastic Wave Scattering, in *Acoustic, Electromagnetic and Elastic Wave Scattering – Focus on the T-matrix Approach* (Pergamon Press Inc., New York, 1980)
20. Ph.M. Morse, H. Feshbach, *Methods of Theoretical Physics* (McGraw-Hill, Inc., New York, 1953)
21. R. Courant, J.D. Hilbert, *Methods of Mathematical Physics* (J. Wiley, New York, 1966)
22. L. Brillouin, *Wave Propagation and Group Velocity* (Academic Press, New York, 1960)
23. G.N. Watson, *Theory of Bessel Functions* (Cambridge University Press, New York, 1966)
24. G.V. Frisk, *Ocean and Seabed Acoustics* (PTR Prentice Hall, New Jersey, 1994)
25. I. Tolstoy, C.S. Clay, *Ocean Acoustics* (AIP, New York, 1987)